AGU PUBLICATIONS

Geochemistry, Geophysics, Geosystems

RESEARCH ARTICLE
10.1002/2017GC006901

Key Points:
- A simplified coupling concept is proposed for modeling geomechanical feedback on gas production behavior of hydrate reservoirs
- Coupling concept is validated by numerical simulation of gas hydrate formation and dissociation in a controlled triaxial compression test
- Coupling concept applies to pore-filling hydrates as well as for hydrates in the transition zone between pore-filling and load-bearing habits

Supporting Information:
- Supporting Information S1
- Data Set S1
- Data Set S2
- Data Set S3
- Data Set S4
- Data Set S5
- Data Set S6

Correspondence to:
S. Gupta,
sgupta@geomar.de

Citation:
Gupta, S., C. Deusner, M. Haeckel, R. Helmig, and B. Wohlmuth (2017), Testing a thermo-chemo-hydro-geomechanical model for gas hydrate-bearing sediments using triaxial compression laboratory experiments, *Geochem. Geophys. Geosyst.*, *18*, 3419–3437, doi:10.1002/2017GC006901.

Received 3 MAR 2017
Accepted 27 JUL 2017
Accepted article online 14 AUG 2017
Published online 13 SEP 2017

Testing a thermo-chemo-hydro-geomechanical model for gas hydrate-bearing sediments using triaxial compression laboratory experiments

S. Gupta[1], C. Deusner[1], M. Haeckel[1], R. Helmig[2], and B. Wohlmuth[3]

[1]Department of Marine Geosystems, Helmholtz Centre for Ocean Research Kiel, Kiel, Germany, [2]Department of Hydromechanics and Modelling of Hydrosystems, University of Stuttgart, Stuttgart, Germany, [3]Chair for Numerical Mathematics, Technical University Munich, Garching bei München, Germany

Abstract Natural gas hydrates are considered a potential resource for gas production on industrial scales. Gas hydrates contribute to the strength and stiffness of the hydrate-bearing sediments. During gas production, the geomechanical stability of the sediment is compromised. Due to the potential geotechnical risks and process management issues, the mechanical behavior of the gas hydrate-bearing sediments needs to be carefully considered. In this study, we describe a coupling concept that simplifies the mathematical description of the complex interactions occurring during gas production by isolating the effects of sediment deformation and hydrate phase changes. Central to this coupling concept is the assumption that the soil grains form the load-bearing solid skeleton, while the gas hydrate enhances the mechanical properties of this skeleton. We focus on testing this coupling concept in capturing the overall impact of geomechanics on gas production behavior though numerical simulation of a high-pressure isotropic compression experiment combined with methane hydrate formation and dissociation. We consider a linear-elastic stress-strain relationship because it is uniquely defined and easy to calibrate. Since, in reality, the geomechanical response of the hydrate-bearing sediment is typically inelastic and is characterized by a significant shear-volumetric coupling, we control the experiment very carefully in order to keep the sample deformations small and well within the assumptions of poroelasticity. The closely coordinated experimental and numerical procedures enable us to validate the proposed simplified geomechanics-to-flow coupling, and set an important precursor toward enhancing our coupled hydro-geomechanical hydrate reservoir simulator with more suitable elastoplastic constitutive models.

1. Introduction

Methane hydrates are crystalline solids formed from water molecules enclathrating methane molecules. Methane hydrates are thermodynamically stable under conditions of low temperatures and high pressures. If warmed or depressurized, methane hydrates destabilize and dissociate into water and methane gas. Natural gas hydrates occur in permafrost regions and the deep sea, usually in soils or sediments at considerable depth when methane is available in sufficient amounts. Natural gas hydrates are considered to be a promising energy resource. It is widely believed that the energy content of methane occurring in hydrate form is immense, possibly exceeding the combined energy content of all other conventional fossil fuels [*Piñero et al.*, 2013; *Burwicz et al.*, 2011; *Archer et al.*, 2009; *Milkov*, 2004; *Kvenvolden*, 1993].

Several methods have been proposed for production of natural gas from gas hydrate reservoirs, e.g., thermal stimulation, depressurization, and chemical activation [*Moridis et al.*, 2009, 2011; *Park et al.*, 2006; *Lee et al.*, 2003]. Currently, depressurization is deemed the most mature approach. Consequently, significant research and development effort has been directed toward assessing the potential of depressurization as a primary driving force for natural gas production from gas hydrate reservoirs. Recent field trials, onshore below the Alaskan permafrost and in the Nankai Trough offshore Japan were both essentially depressurization tests; the Japanese test used only depressurization [*Yamamoto*, 2013, 2015; *David*, 2013], while, the Alaskan test was combined with N_2:CO_2 injection [*Anderson et al.*, 2014; *Schoderbek et al.*, 2013].

In the earlier gas production studies, several mathematical models [e.g., *Tsypkin*, 1991; *Ahmadi et al.*, 2004; *Yousif*, 1991; *Sun et al.*, 2005; *Liu and Flemings*, 2007; *Moridis*, 2003; *Moridis et al.*, 2007] and numerical

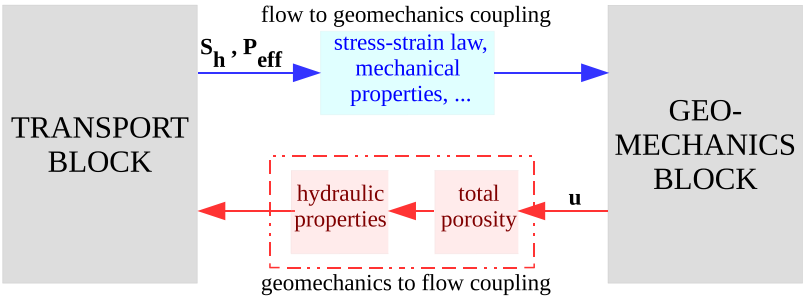

Figure 1. Coupling concept.

simulators (e.g., MH21-HYDRES *Kurihara et al*. [2009], STOMP-HYD *White and McGrail* [2006], UMSICHT HyRes *Janicki et al*. [2011], and TOUGH-HYDRATE *Moridis et al*. [2008]) were developed, which focused on hydrate phase change and fluid flow rather than on the geomechanical behavior. Over the years, it has become increasingly clear that the geomechanical effects associated with these gas production methods cannot be ignored. Recent field trials have shown that large deformation and sand production are relevant risks for natural gas production from gas hydrate-bearing sediments [*Schoderbek et al*., 2013; *Yamamoto*, 2013, 2015], and reliable simulation tools are needed for risk assessment and production strategy development. Coupling between solid deformation and fluid transport lays the foundation for the simulation of the thermo-hydro-chemo-mechanical behavior of gas hydrate-bearing sediment during gas production, and the experimental validation of the coupling relationships is extremely important for adding certainty to predictive simulation of production scenarios and sediment mechanical behavior in general. Several mathematical and numerical tools [e.g., *Klar et al*., 2010; *Kimoto et al*., 2010; *Rutqvist*, 2011; *Hyodo et al*., 2014; *Gupta et al*., 2015] have since been developed to study gas production in gas hydrate reservoirs in a coupled thermo-chemo-hydro-geomechanical framework.

In a typical gas hydrate reservoir, the structure of the sediment is expected to change due to two distinct effects: (1) the changing hydrate saturation, and (2) the sediment deformation. What complicates the matter further is that the hydrate provides additional strength to the sediment through a cementation-like effect, thereby, effectively coupling the two inputs; hydrate saturation, and sediment deformation. For any detailed hydro-geomechanical description of the gas production from gas hydrate-bearing sediments, it is imperative to analyze how the transport processes (i.e., flow and chemical processes) would respond to any given geomechanical input. As can be expected, this is a rather challenging task due to the complexity of the interactions. In our model, we simplify the mathematical description of the coupled hydro-geomechanical processes by conceptualizing that the model can be decomposed into two distinct model blocks: transport-block and geomechanics-block, with the coupling between the two manifesting as changes in properties of each model block (see Figure 1). The transport-block solves for the hydrate phase change and the nonisothermal, two-phase, two-component flow of water and methane gas, while the geomechanics-block solves for the sediment displacements. This decomposition is based on the simplifying assumption that the soil grains constitute the skeleton of the porous matrix, while the gas hydrate enhances the mechanical properties of this skeleton without actively bearing the load. The relative deformation of the gas hydrate phase with respect to the soil skeleton is ignored. This assumption allows us to distinguish between the *total porosity* and the *apparent porosity*. The total porosity characterizes the total pore volume, i.e., the volume not occupied by the soil grains, while the apparent porosity characterizes the actual pore volume which is available for the fluid flow. The deformation of the hydrate-bearing sediment directly affects only the total porosity. The evolution of the actual or apparent porosity field is then modeled by scaling the total porosity with functions of hydrate saturation through simple geometric arguments. To make the physical meaning clear, the apparent porosity is the actual measured quantity, while the total porosity is a mathematical construct which allows us to isolate the effects of sediment deformation from those of hydrate phase change. We also assume that those properties of the transport-block which depend on the sediment structure (i.e., hydraulic properties like permeability, capillary pressure, specific surface area, tortuosity, etc.) can be modeled as a *multiplicative decomposition* of functions of total porosity and hydrate saturation. In effect, with these simplifications, we can describe all feedback from geomechanics-block to the transport-block through a single transfer variable: total porosity, and this forms a central feature of our coupling concept.

In this study, through numerical simulation of a highly controlled high-pressure triaxial experiment combined with methane hydrate formation and dissociation, we aim to establish whether this coupling concept is effective in capturing the overall impact of geomechanics on the gas production behavior.

To be able to test the coupling with confidence, there are two important prerequisites: (1) a well-tested model for the transport-block, and (2) a good enough estimation of the displacement field. The validation of the transport-block in our hydrate reservoir model was performed in our earlier study [*Gupta et al*., 2015]. For the second prerequisite, however, we require a suitable constitutive model for describing the stress-strain response of the hydrate-bearing sediment. A number of nonlinear elastic [e.g., *Yu et al*., 2011; *Miyazaki et al*., 2011a,], elastoplastic [e.g., *Klar et al*., 2010; *Uchida et al*., 2012; *Sun et al*., 2015; *Lin et al*., 2015], and elastoviscoplastic [e.g. *Kimoto et al*., 2010] constitutive models have been proposed in the recent years to model the geomechanical behavior of gas hydrate-bearing sediments. The stress strain relation in these models is quite complex. Variationally consistent formulations result in nonlinear and nonsmooth inequality settings. These can be reformulated in terms of nonlinear complementarity functions to which semismooth Newton algorithms as iterative solvers can be applied, which converge locally. To enlarge the local convergence radius, suitable regularization and damping strategies can be designed [*Hager and Wohlmuth*, 2009, 2010]. Only in special situations existence and uniqueness is given, and often, only local existence is guaranteed and path dependent solutions exist. We refer to *Mielke* [2004, 2009] and the references therein for existence results at finite strain. However, none of these results can be directly applied to our setting since we have a fully coupled hydrate system involving more nonlinearities in the bidirectional couplings. Additionally, the constraints of the system involve inequalities which are nonlinear and nonsmooth, leading to a model with a large number of parameters which often makes model calibration challenging and unreliable. To the best of our knowledge, none of these models have been validated in coupled hydro-geomechanical settings in the context of gas production from gas hydrate reservoirs, and have a large uncertainty associated with their predictive capabilities in highly dynamic conditions. In this study, it is of particular interest to reduce the complexity of the geomechanics-block as much as possible in order to reduce the uncertainty associated with the choice of a constitutive model. We, therefore, chose a uniquely invertible linear-elastic constitutive model in the geomechanics-block of our hydrate reservoir model. We account for the stiffening effect due to gas hydrates by parameterizing the Young's modulus as a function of hydrate saturation S_h [*Santamarina and Ruppel*, 2010]. We also account for material compressibility with respect to hydrostatic pressure. The pressure dependence of compressibility and the S_h dependence of Lames parameters introduces a weak nonlinearity in the geomechanics-block. The numerical implementation of the poroelastic model and the transport-to-geomechanics coupling in our hydrate reservoir model was also validated in our earlier study [*Gupta et al*., 2015].

In general, poroelasticity is not a realistic model for the geomechanical description of cemented granular materials where the stress-strain response is typically nonlinear, and the shear-volumetric coupling (dilatancy) is of particular importance. Therefore, in order to validate our coupling concept within the constraints stated above, we control our triaxial experiment very carefully in a way that ensures that the assumptions of poroelasticity remain valid throughout the periods of interest for numerical simulation.

2. Hydrate Reservoir Model

2.1. Mathematical Model

Our model considers kinetic hydrate phase change and nonisothermal, multiphase, multicomponent fluid flow through poroelastic porous medium. The model assumes that the porous medium is composed of three *components*: CH_4, H_2O, and methane hydrate ($CH_4 \cdot N_h H_2O$), which are present in three distinct *phases*: gaseous, aqueous, and solid. The gaseous phase comprises of methane gas and water vapor. The aqueous phase comprises of water and dissolved methane. The solid phase comprises of pure methane hydrate and sand grains. The sand grains are assumed to form a material continuum which provides the skeletal structure to the porous medium. We shall refer to this as *solid matrix*. The aqueous, gaseous, and hydrate phases exist in the void spaces of this solid matrix (see Figure 2).

We assume that the hydrate cements the sand grains in the mechanical sense (i.e., without forming any chemical bonds), such that the sand and hydrate together form a *composite solid matrix*. The relative deformation of the gas hydrate phase with respect to the soil skeleton is ignored. This assumption allows us to

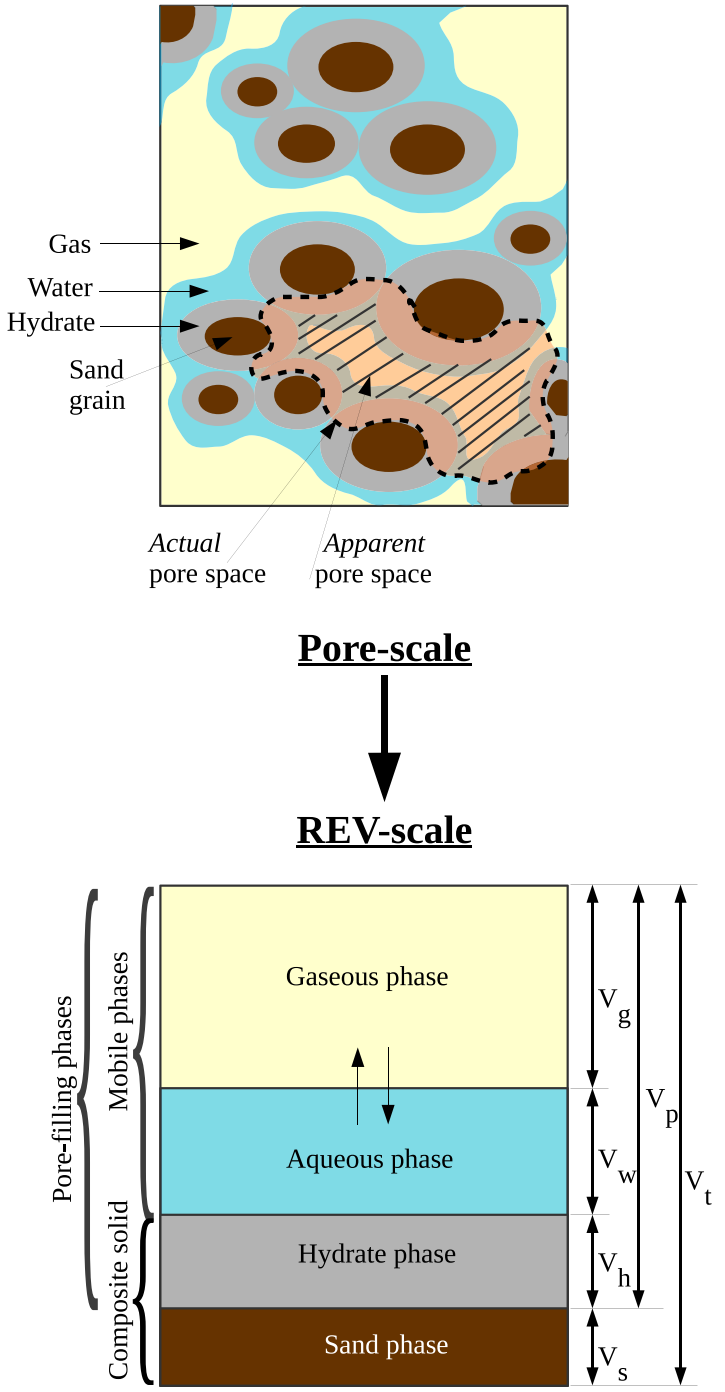

Figure 2. Pore-scale to REV-scale.

write a single momentum balance equation for the composite solid phase, instead of separate ones for the sand and the hydrate phases each. To describe the mechanical behavior of the composite solid matrix, we make a further simplifying assumption that the sand grains form the primary load-bearing structure, while the hydrates enhance the mechanical strength and stiffness of this structure without bearing any load themselves. This assumption is also adopted even after hydrate-bearing soil is loaded during depressurization. Because of this, the constitutive law does not consider stress-relaxation term that accounts for the release of load that has been carried by hydrates as introduced by others [*Klar et al.*, 2010; *Uchida et al.*, 2012].

We decompose the mathematical model into transport and geomechanics blocks, and isolate the effects of hydrate phase change and ground deformation through the introduction of the variable *total porosity*. This is justified based on the above assumption that the soil grains constitute the primary load-bearing skeleton of the porous matrix, such that deformation of the hydrate-bearing sediment directly affects only the total porosity. This assumption allows us to solve for the mass balance of soil and hydrates separately, thus conveniently separating hydrate phase change kinetics from sediment deformation. If, for example, we do not make this assumption, then we would have to solve for the mass balance of soil and hydrate as a single composite phase leading to a strong coupling between hydrate phase change and geomechanics. The model decomposition would not be straightforward in this case, and the evolution of porosity field would be very complex, making the description of the fluid flow and the evolution of the hydraulic properties also significantly more challenging. One clear advantage of this simplification is that it gives a very modular structure to the model, with each model-block operating independently, and communicating with each other through coupling relationships which are neatly resolved with respect to the independent output variables of each model-block (see Figure 1). Another important advantage is that the model decomposition allows us to use multirate time-stepping schemes, as discussed in *Gupta et al*. [2016], which can significantly speed up the calculation, especially for 3-D problems.

The mathematical model is described in detail in *Gupta et al*. [2015]. A summary of the governing equations and the constitutive relationships are given in Table 1. The phases occupying the pore space (gaseous, aqueous, hydrate) are denoted by "β"$=g,w,h$ respectively, the mobile phases (gaseous and aqueous) are denoted by "α" $=g,w$, and the mobile molecular components are denoted by "κ" $=CH_4,H_2O$. The solid matrix is designated with the subscript "*s*." The sand + hydrate composite solid matrix is designated with the subscript "*sh*." "γ" is used to denote all phases, i.e., $\gamma=g,w,h$, and *s*.

2.2. Primary Variables

The mathematical model consists of the following six governing equations: the mass balance equations (1)–(4), the momentum balance equation (7) for the composite-solid, and the energy balance equation (8). The momentum balance equations (5) and (6) for the mobile phases $\alpha=g,w$ give the α-phase velocities directly, and are thus absorbed in the mass and energy balance equations. We chose the following set of variables as the primary variables: the gas phase pressure P_g, the aqueous phase saturation S_w, the hydrate phase saturation S_h, the temperature T, the total-porosity ϕ, and, the composite-matrix displacement $\mathbf{u}$. All other variables can be derived (explicitly or implicitly) from this set of variables using the closure and constitutive relationships.

2.3. Solution Strategy

We use an iteratively coupled solution strategy. The mathematical model is decomposed into three parts:

1. transport-block ($\mathbf{F_f}$), comprised of the mass balance equations for CH_4, H_2O, and Hydrate, and the energy balance equation,
2. geomechanical-block ($\mathbf{F_g}$), comprised of the momentum balance equation for composite solid phase, and
3. porosity-equation ($\mathbf{F}_\phi$), comprised of the mass balance equation for the sand phase.

$\mathbf{F_f}$ is solved for the variables P_g, S_w, S_h, and T, $\mathbf{F_g}$ is solved for displacements $\mathbf{u}$, and $\mathbf{F}_\phi$ is solved for total porosity ϕ. $\mathbf{F_f}$ and $\mathbf{F}_\phi$ are spatially discretized using a fully upwinded cell-centered finite volume method. Orthogonal grids aligned with the principal axes are defined and a control-volume formulation with two-point flux approximation (TPFA) is used. $\mathbf{F_g}$ is discretized using Galerkin finite element (FEM) method defined on $Q1$ elements. An implicit Euler time-stepping scheme is used for marching forward in time. The solution for a given time step involves two iterative loops, the *inner loop* and the *outer loop*. The *inner loop* uses Newton's method and SuperLU [*Demmel et al*., 1999] linear solver to solve each of $\mathbf{F_f}$, $\mathbf{F_g}$, and $\mathbf{F}_\phi$, thus taking care of the decoupled solution. The *outer loop* reintroduces the coupling between $\mathbf{F_f}$, $\mathbf{F_g}$, and $\mathbf{F}_\phi$ through a block Gauss Seidel iterative scheme.

The numerical scheme is implemented in the C++ based DUNE-PDELab framework [*Dedner et al*., 2012], and is capable of solving problems in 1-D, 2-D, and 3-D domains.

Table 1. Summary of the Mathematical Model

Governing Equations		Equation No.
Mass balance for each mobile component $\kappa = CH_4, H_2O$	$\sum_\alpha \left[\partial_t\left(\phi\,\rho_\alpha\,\chi_\alpha^\kappa\,S_\alpha\right)\right] + \sum_\alpha \left[\nabla\cdot\left(\phi\,\rho_\alpha\,\chi_\alpha^\kappa\,S_\alpha\,\mathbf{v}_{\alpha,t}\right)\right] = \sum_\alpha \left[\nabla\cdot\left(\phi\,S_\alpha\,\mathbf{J}_\alpha^\kappa\right)\right] + \dot{g}^\kappa + \sum_\alpha \dot{q}_{m_\alpha}^\kappa + \dot{S}_{ext}^\kappa$	(1),(2)
Mass balance for hydrate phase	$\partial_t\left(\phi\,\rho_h\,S_h\right) + \nabla\cdot\left(\phi\,\rho_h\,S_h\,\mathbf{v}_{h,t}\right) = \dot{g}^h$	(3)
Mass balance for sand phase	$\partial_t\left[(1-\phi)\,\rho_s\right] + \nabla\cdot\left((1-\phi)\,\rho_s\,\mathbf{v}_s\right) = 0$	(4)
Momentum balance for mobile phases $\alpha = g, w$	$\mathbf{v}_\alpha = -K\,\frac{k_{r\alpha}}{\mu_\alpha}\left(\nabla P_\alpha - \rho_\alpha\,\mathbf{g}\right)$ (Darcy's Law)	(5),(6)
Momentum balance for composite-solid	$\nabla\cdot\tilde{\sigma} + \rho_m\,\mathbf{g} = 0$ where, ρ_m is the bulk density given by $\rho_m = \sum_\beta \left(\phi\,S_\beta\,\rho_\beta\right) + (1-\phi)\rho_s$	(7)
Energy balance	$\partial_t\left[(1-\phi)\rho_s u_s + \sum_\beta \left(\phi\,S_\beta\,\rho_\beta\,u_\beta\right)\right] + \sum_\alpha \left[\nabla\cdot\left(\phi\,\rho_\alpha\,\chi_\alpha^\kappa\,S_\alpha\,\mathbf{v}_{\alpha,t}\,h_\alpha\right)\right] = \nabla\cdot k_{eff}^c\nabla T + \dot{Q}_h + \sum_\alpha \left(\dot{q}_{m_\alpha}^\kappa\,h_\alpha\right)$ where, $k_{eff}^c = (1-\phi)k_s^c + \sum_\alpha\sum_\kappa \left(\phi\,\chi_\alpha^\kappa\,S_\alpha\,k_\alpha^c\right) + \phi\,S_h\,k_h^c$ $h_\alpha = \int_{T_{ref}}^{T} Cp_\alpha\,dT$ $u_\gamma = \int_{T_{ref}}^{T} Cv_\gamma\,dT$	(8)
Closure relationships		
Relationship between phase pressures	$P_g - P_w = P_c(S_{we})$	(9)
Summation relationships	$\sum_\beta S_\beta = 1$	(10)
	$\forall\alpha: \sum_\kappa \chi_\alpha^\kappa = 1$	(11),(12)
Constitutive relationships		
1. Vapor-liquid equilibrium		
Using Henry's Law and Raoult's Law for ideal gas-liquid solutions,		
For dissolved methane:	$\chi_w^{CH_4} = H(T)\,\chi_g^{CH_4}\,P_g$	
For water vapor:	$\chi_g^{H_2O} = \chi_w^{H_2O}\,\frac{P_{H_2O}^{sat}(T)}{P_g}$	
	where, $H(T)$ is the Henry's constant for methane dissolved in water calculated using the empirical relation from NIST database [*Sander*, 2015], and $P_{H_2O}^{sat}$ is saturated water vapor pressure calculated using Antoine's equation.	
2. Diffusive mass-transfer flux		
Fick's law:	$\mathbf{J}_\alpha^\kappa = -\tau D^\alpha\left(\rho_\alpha\nabla\chi_\alpha^\kappa\right)$	
	where, D^α is the binary diffusion coefficient. D^g is estimated using the empirical relationship proposed by *Stattery and Bird* [1958] for low density binary $CH_4 - H_2O$ system. D^w is estimated using the Wilke-Chang correlation [*Himmelblau*, 1964] for dilute associated liquid mixtures is used.	
3. Hydrate phase change kinetics		
Nonequilibrium phase change of methane hydrate is modeled by the Kim-Bishnoi kinetic model [*Kim et al.*, 1987].		
Gas generation rate	$\dot{g}^{CH_4} = k_{reac}\,M_{CH_4}\,A_{rs}\left(P_e - f_g\right)$	(13)
	where, k_{reac} is the rate of kinetic phase-change, P_e is the hydrate equilibrium pressure, modeled as [*Kamath*, 1984],	
	$P_e = A_1\exp\left(A_2 - \frac{A_3}{T}\right)$,	(14)
	f_g is the gas fugacity calculated using the Peng-Robinson EoS for methane gas, and, A_{rs} is the specific reaction surface area modeled as $A_{rs} = \Gamma_r A_s$, where, A_s is the total surface area and Γ_r is the ratio of the active reaction surface to the total surface area. A_s and Γ_r are modeled using the correlations proposed by *Yousif* [1991] and *Sun and Mohanty* [2006], respectively.	
Water generation rate	$\dot{g}^{H_2O} = \dot{g}^{CH_4}\,N_{Hyd}\,\frac{M_{H_2O}}{M_{CH_4}}$	(15)
Hydrate consumption rate	$-\dot{g}^{Hyd} = \dot{g}^{CH_4}\,\frac{M_{Hyd}}{M_{CH_4}}$	(16)
Heat of hydrate dissociation	$\dot{Q}_h = \frac{-\dot{g}^{Hyd}}{M_{Hyd}}\left(B_1 - \frac{B_2}{T}\right)$	(17)
4. Properties of the fluid-matrix interaction		
Capillary pressure	$P_c = P_{c0}\cdot f_{S_h}^{Pc}(S_h)\cdot f_\phi^{Pc}(\phi)$	(18)
	where, P_{c0} is capillary pressure for undeformed, unhydrated solid matrix, given by Brooks-Corey relationship,	
	$P_{c0} = P_{entry}\,S_{we}^{-1/\lambda_{BC}}$,	(19)
	and, $f_{S_h}^{Pc}(S_h)$ and $f_\phi^{Pc}(\phi)$ are scaling factors to account for the effects of S_h [*Rockhold et al.*, 2002] and ϕ (*Civan*'s power law correlation *Civan* [2000]) respectively,	
	$f_{S_h}^{Pc} = (1-S_h)^{-\frac{3\lambda_{BC}-1}{3\lambda_{BC}}}$ and, $f_\phi^{Pc} = \frac{\phi_0}{\phi}\left(\frac{1-\phi}{1-\phi_0}\right)^2$	(20)
Intrinsic permeability	$K = K_0\cdot f_{S_h}^K(S_h)\cdot f_\phi^K(\phi)$	(21)

Table 1. (continued)

Governing Equations		Equation No.
	where, K_0 is intrinsic permeability of the undeformed, unhydrated solid matrix, and, $f^K_{S_h}(S_h)$ and $f^K_{\phi}(\phi)$ are scaling factors to account for the effects of S_h [*Rockhold et al*., 2002] and ϕ [*Civan*, 2000] respectively,	
	$f^K_{S_h}=(1-S_h)^{\frac{19}{6}}$ and, $f^K_{\phi}=\frac{\phi}{\phi_0}\left(f^{Pc}_{\phi}\right)^{-2}$	(22)
Relative permeabilities	Relative permeabilities of the mobile phases are modeled using Brooks-Corey model in conjunction with the Burdine theorem [*Burdine*, 1953], as	
	$k_{rw}=S_{we}^{\frac{2+3\lambda_{BC}}{\lambda_{BC}}}$ and, $k_{rg}=(1-S_{we})^2\left(1-S_{we}^{\frac{2+\lambda_{BC}}{\lambda_{BC}}}\right)$ where, $S_{we}=\frac{S_w}{1-S_h}$	(23)
Hydraulic tortuosity	$\tau=\phi^n$ where, $1\leq n\leq 3$	(24)
5. Poro-elasticity		
Effective stress principle	Effective stress concept introduced by *Terzaghi* [1925] and modified by *Biot* [1941] is used.	
	$\tilde{\sigma}=\tilde{\sigma}'+\alpha_{biot}\left(\frac{S_g P_g+S_w P_w}{S_g+S_w}\right)\tilde{I}$	(25)
	where, $\tilde{\sigma}$ is the total stress acting on the bulk porous medium, and $\tilde{\sigma}'$ is the effective stress acting on the composite skeleton.	
	α_{biot} is the Biot-Willis constant [*Biot and Willis*, 1957].	
Linear elastic law	$\tilde{\sigma}'=2G_{sh}\,\tilde{\epsilon}+\lambda_{sh}(tr\,\tilde{\epsilon})\,\tilde{I}$	(26)
	where, $\tilde{\epsilon}$ is the linearized strain, given by $\tilde{\epsilon}=\frac{1}{2}(\nabla\mathbf{u}+\nabla^T\mathbf{u})$	(27)
	and, G_{sh} and λ_{sh} are the Lame's parameters.	
Young's modulus	Young's modulus E_{sh} is modeled using the parameterization proposed by *Santamarina and Ruppel* [2010]: $E_{sh}=E_s+S_h^c E_h$	
	where, E_s and E_h are the Young's modulus of hydrate-free sand and hydrate, respectively.	(28)

3. Material and Methods

We performed a controlled triaxial volumetric strain test on a sand sample in which methane hydrate was first formed under controlled effective stress and then dissociated via depressurization under controlled total stress. Gas hydrate in our experiment was initially formed by pressurizing partially water-saturated sand with gaseous methane to reach a gas hydrate saturation of 0.4, and remaining methane gas was replaced with seawater before the sample was depressurized stepwise. Confining and axial loads in the triaxial testing were applied isotropically and were carefully controlled to keep the deformation of the sample small and well within the assumptions of poroelasticity.

3.1. Experimental Setup and Components

Experiments were carried out in the custom-made high-pressure apparatus NESSI (Natural Environment Simulator for Subseafloor Interactions) [*Deusner et al*., 2012], which is equipped with a triaxial cell mounted in a 40 L stainless steel vessel (APS GmbH Wille Geotechnik, Rosdorf, Germany). The sample sleeve is made from FKM, other wetted parts of the setup are made of stainless steel. Salt water medium was stored in reservoir bottles (DURAN, Wertheim, Germany) prior to use in experiments, and the seawater medium was pressurized in an additional pressure vessel (Parr Instrument GmbH, Frankfurt, Germany) to allow fast transfer into the sample vessel. Fluid pressure in the sample vessel was adjusted with a back-pressure regulator valve (TESCOM Europe, Selmsdorf, Germany). Experiments were carried out in upflow mode with injection of CH_4 gas and seawater medium at the bottom of the sample prior to and after gas hydrate formation (Figure 3a), respectively, and fluid discharge at the top of the sample during depressurization (Figure 3b). Axial and confining stresses, and the sample volume changes were monitored throughout the experimental period. Axial and confining stresses were controlled using high-precision hydraulic pumps and actuators (VPC 400, APS GmbH Wille Geotechnik, Rosdorf, Germany), and changes in hydraulic fluid volumes were converted to calculate sample volume changes. Pore pressure was measured in the influent and the effluent fluid streams close to the sample top and bottom. The experiment was carried out under constant temperature conditions. Temperature control was achieved with a thermostat system (T1200, Lauda, Lauda-Königshofen, Germany). Produced gas mass flow was analyzed with mass flow controllers (EL FLOW, Bronkhorst, Kamen, Germany). For control purposes, bulk effluent fluids were also collected inside 100 L gas tight TEDLAR sampling bags (CEL Scientific, Santa Fe Springs CA, USA). The sampling bags were mounted inside water filled containers. After expansion of the effluent fluids at atmospheric pressure, the overall volume was measured as volume of water displaced from these containers.

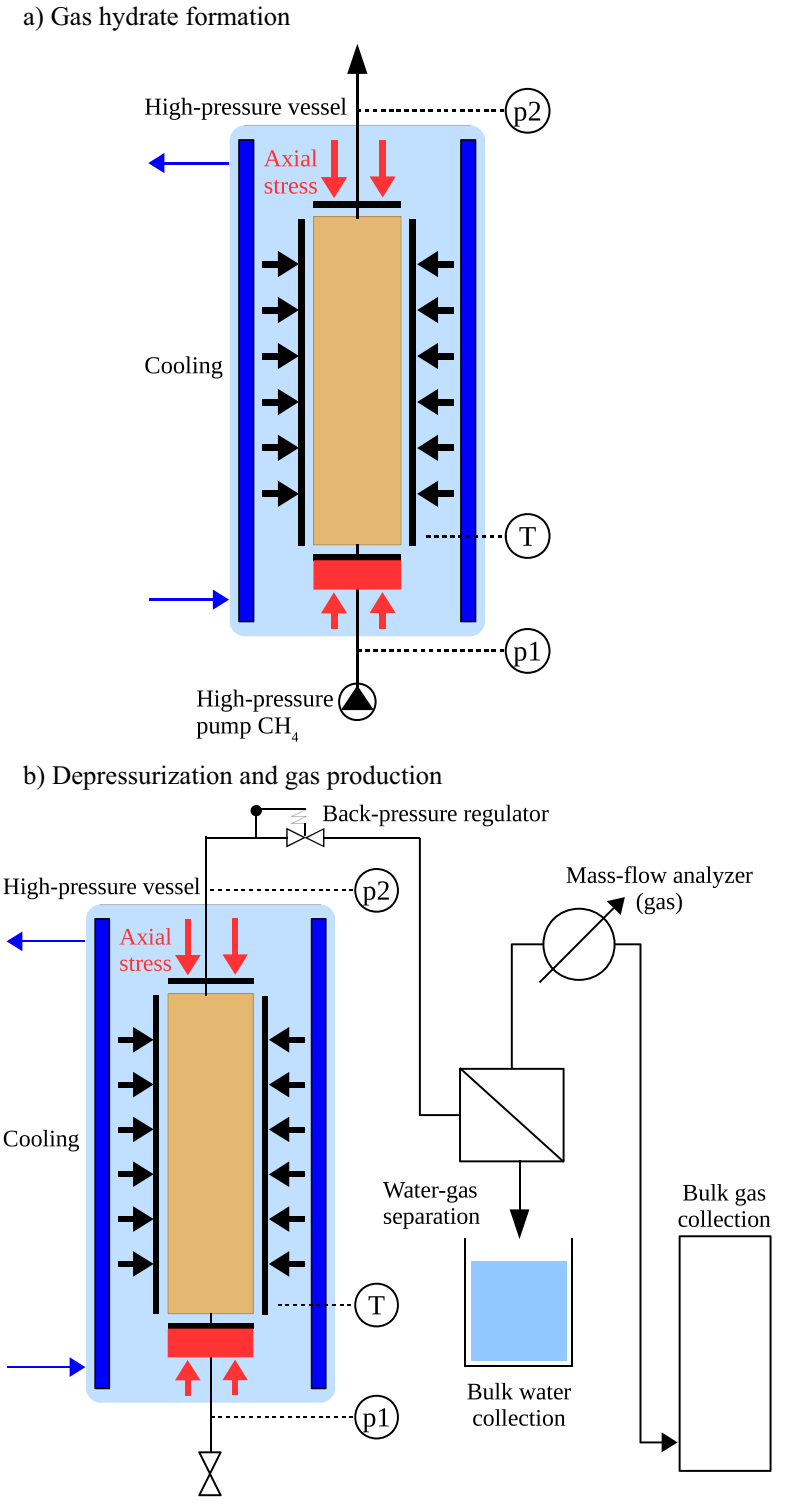

Figure 3. Simplified flow schemes for relevant period. (a) Gas hydrate formation. (b) Depressurization and gas production.

3.2. Sample Preparation and Mounting

The sediment sample was prepared from quartz sand (initial sample porosity: 0.35, grain size: 0.1−0.6 mm, G20TEAS, Schlingmeier, Schwülper, Germany), which was mixed with deionized water to achieve a final water saturation of 0.4 relative to the initial sample porosity. The partially water-saturated and thoroughly

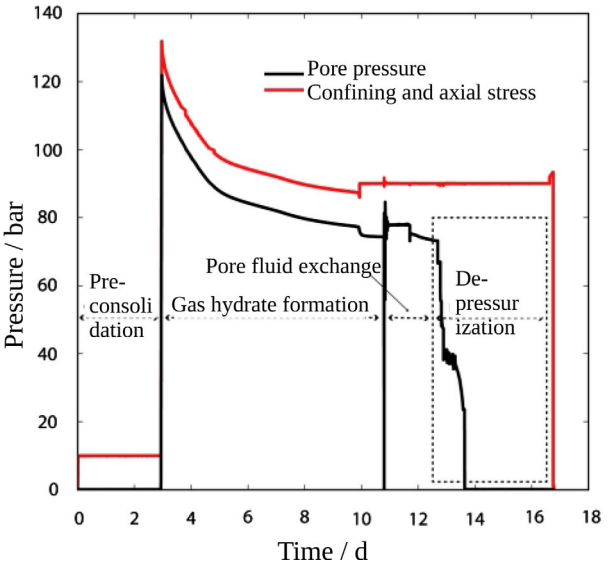

Figure 4. Overview of the *measured* pressure and stresses over time.

homogenized sediment was filled into the triaxial sample cell to obtain final sample dimensions of 360 mm in height and 80 mm in diameter. The sample geometry was assured using a sample forming device. The sample was cooled to 2°C after the triaxial cell was mounted inside the pressure vessel. Initial water permeability of the gas hydrate-free sediment was estimated to be 5×10^{-10} m^2.

3.3. Experimental Procedure

3.3.1. Gas Hydrate Formation

Prior to the gas hydrate formation, the partially water-saturated sediment sample was isotropically consolidated to 1 MPa effective stress under drained conditions. It should be noted that the apparent effective stress is monitored and controlled as differential pressure between the confining hydraulic fluid pressure of the reactor and the gas pressure in the sample pore space. Measurements and control algorithms do not take into account the changes in effective stress due to changes in water saturation and capillary pressure. Thus, only the apparent effective stress is directly accessible from experimental procedures. The sample was flushed with CH_4 gas to replace air with methane. The sample was, subsequently, pressurized with CH_4 gas to approximately 12.5 MPa (Figure 3a). During pressurization with CH_4 gas and throughout the overall gas hydrate formation period, formation stress condition of 1 MPa effective stress were maintained using an automated control algorithm. The formation process was continuously monitored by logging the CH_4 gas pressure. Mass balances and volume saturations were calculated based on CH_4 gas pressure and initial mass and volume values. Gas hydrate formation was terminated after 1.84 mol of CH_4-hydrate had been formed after approximately 6 days, corresponding to CH4-hydrate saturation of 0.39. The sample was cooled to −5°C and stress control was switched to constant total isotropic stress control at approximately 9 MPa before the sample pore space was depressurized to atmospheric pressure and the remaining CH_4 gas in the pore space was released. System repressurization and water saturation of the pore space was achieved by instant filling and repressurization with pre-cooled −1°C saltwater medium according to the seawater composition. Hydrate dissociation during the brief period of depressurization was minimized by taking advantage of the anomalous self-preservation effect, which reaches an optimum close to the chosen temperature [*Stern et al.*, 2003]. After completion of the gas-water fluid exchange, the sample temperature was readjusted to 2°C.

3.3.2. Depressurization and Gas Production

The sample pore space was depressurized and gas produced by stepwise decrease of back pressure at constant isotropic total stress (Figure 3b). Overall fluid production (water and CH_4 gas) was monitored after depressurization at atmospheric pressure after temperature equilibration.

4. Numerical Simulation

The overall experiment was carried out in four steps, viz., (1) *preconsolidation*, (2) *gas hydrate formation*, (3) *pore-fluid exchange*, and (4) *depressurization*, as described in section 3. During steps 1 and 2, the sample was maintained under a defined effective loading with the confining and the axial stresses were controlled to remain 10 bar above the pore pressure. During steps 3 and 4, the total isotropic stress was controlled to remain at a constant level (see Figure 4). The experiment was performed over a total period of about 16.8 days. The *periods of interest* for this simulation are: (1) from *Day* – 3 to *Day* – 10, corresponding to gas hydrate formation, and (2) from *Day*-12.8 to *Day*-13.8, corresponding to depressurization and gas production. We simulate both of these periods separately.

Table 2. Material Properties and Model Parameters

				Ref.
Thermal Conductivities				
k_g^c		$-0.886\times10^{-2}+0.242\times10^{-3}T-0.699\times10^{-6}T^2+0.122\times10^{-8}T^3$	$W\cdot m^{-1}\cdot K^{-1}$	*Roder* [1985]
k_w^c		$0.3834\ln(T)-1.581$	$W\cdot m^{-1}\cdot K^{-1}$	*Wagner and Kretzschmar* [2008]
k_h^c		2.1	$W\cdot m^{-1}\cdot K^{-1}$	*Sloan and Koh* [2007]
k_s^c		1.9	$W\cdot m^{-1}\cdot K^{-1}$	*Esmaeilzadeh et al.* [2008]
Specific heat capacities				
Cp_g		$\Delta Cp_g^{res}(1238+3.13T+7.9\times10^{-4}T^2-6.86\times10^{-7}T^3)$	$J\cdot kg^{-1}\cdot K^{-1}$	*Peng and Robinson* [1976]; *Esmaeilzadeh et al.* [2008]
Cv_g		$Cp_g+R_{CH_4}$	$J\cdot kg^{-1}\cdot K^{-1}$	
Cp_w		4186	$J\cdot kg^{-1}\cdot K^{-1}$	*Wagner and Kretzschmar* [2008]
Cv_w		$Cp_w+R_{H_2O}$	$J\cdot kg^{-1}\cdot K^{-1}$	
Cv_h		2700	$J\cdot kg^{-1}\cdot K^{-1}$	*Sloan and Koh* [2007]
Cv_s		800	$J\cdot kg^{-1}\cdot K^{-1}$	*Esmaeilzadeh et al.* [2008]
Dynamic viscosities				
μ_g		$10.4\times10^{-6}\left(\frac{273.15+162}{T+162}\right)\left(\frac{T}{273.15}\right)^{1.5}$	Pa·s	*Friend et al.* [1989]
μ_w		$0.001792\exp\left[-1.94-4.80\left(\frac{273.15}{T}\right)+6.74\left(\frac{273.15}{T}\right)^2\right]$	Pa·s	*Wagner and Kretzschmar* [2008]
Densities				
ρ_g		$\frac{P_g}{2R_gT}$	$kg\cdot m^{-3}$	*Peng and Robinson* [1976]
ρ_w		vapor: $0.0022\frac{P_g}{T}$	$kg\cdot m^{-3}$	*Wagner and Kretzschmar* [2008]
		liquid: 1000	$kg\cdot m^{-3}$	*Wagner and Kretzschmar* [2008]
ρ_h		900	$kg\cdot m^{-3}$	*Sloan and Koh* [2007]
ρ_s		2100	$kg\cdot m^{-3}$	
Hydraulic properties				
λ_{BC}		1.2		*Helmig* [2016]
P_{entry}		50	kPa	*Helmig* [2016]
Hydrate kinetics				
k_{reac}		Formation: 0.2×10^{-11} Dissociation: 3.2×10^{-10}	$mol\cdot m^{-2}\cdot Pa^{-1}\cdot s^{-1}$	
N_{Hyd}		5.75		
$P_{e,0}$		$A_1=10^6$, $A_2=38.98$, $A_3=8533.8$	Pa	*Kamath and Holder* [1987]
$\dot{Q}_h$		$B_1=56599$, $B_2=16.744$	$W\cdot m^{-3}$	*Esmaeilzadeh et al.* [2008]
Poroelasticity parameters				
α_{biot}		0.8		*Verruijt* [2008]
ν_{sh}		0.15		*Miyazaki et al.* [2011b]
	Formation	dissociation		
E_s	32	160	MPa	
E_h	250	360	MPa	
c	1	3		

4.1. Computational Domain

Assuming that the sand sample is axially symmetric, a 2-D radial plane of dimensions 360 mm × 40 mm is chosen as the computational domain. The dimensions correspond to the physical size of the sample. The domain is discretized into 72 × 8 cells.

4.2. Test-setting

4.2.1. Gas Hydrate Formation Period

The schematic of the hydrate formation test is shown in Figure 5. The schematic also shows the initial and boundary conditions. The simulation is run until t_{end} = 604,800 s (i.e., 7 days) using a maximum time step size of 120 s.

4.2.2. Depressurization and Gas Production Period

The schematic of the depressurization test is shown in Figure 6. The schematic also shows the initial and boundary conditions. The simulation is run until t_{end} = 86,400 s (i.e., 1 day) using a maximum time step size of 120 s.

4.3. Properties and Parameters

The material properties and model parameters chosen for this simulation are listed in Table 2. The values of the thermal conductivities, specific heat capacities, dynamic viscosities, and densities for each phase are chosen from standard literature, the references to which are included in the table. The Brooks-Corey parameters are chosen from the range of typically expected values for sand samples.

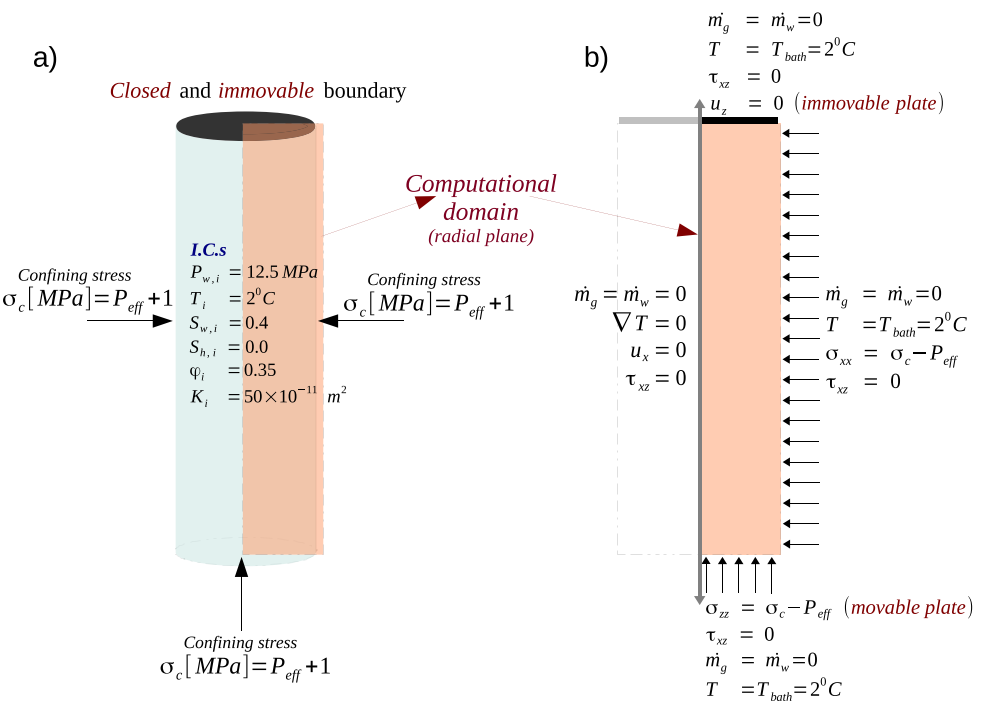

Figure 5. Test setting for the **gas hydrate formation** period. (a) The sample and the initial conditions, and (b) the 2-D computational domain and the boundary conditions.

The most important properties and parameters relevant to the simulation of the experimental data arise from (1) the hydrate-phase-change kinetics, and (2) the poroelastic behavior of the hydrate-bearing sediments.

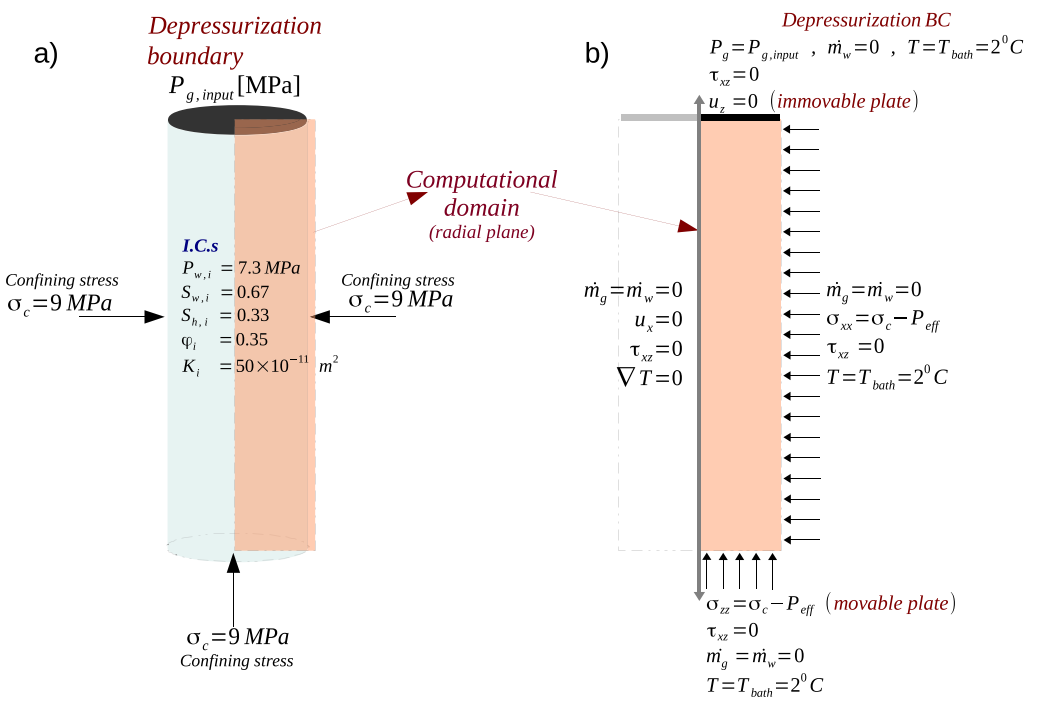

Figure 6. Test setting for the **depressurization and gas production** period. (a) The sample and the initial conditions, and (b) the 2-D computational domain and the boundary conditions.

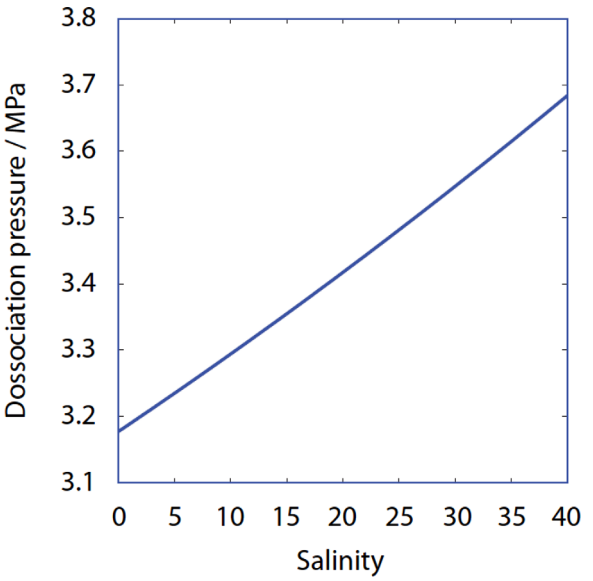

Figure 7. Effect of salinity on hydrate stability curve (at $T_{bath}=2^{\circ}C$).

The hydrate phase-change is modeled by equations (13), (15)–(17). The hydrate-phase equilibrium pressure P_e in equation (13) is modeled in accordance with the findings of *Kamath* [1984]. For hydrates in pure water, the equilibrium pressure depends only on the temperature. However, for hydrates in sea water (which is the case for our sample), the equilibrium pressure also depends on the salinity, as shown in Figure 7. We account for the effect of salinity on the hydrate equilibrium pressure through linear curve fitting on dissociation pressure versus salinity curve.

The reaction surface area, A_{rs}, in equation (13), describes the surface area available for the kinetic-reaction, and puts a limit on the mass transfer during hydrate formation and dissociation. As the hydrate saturation in the pore-space increases, the availability of free surface for hydrate formation to occur decreases, and vice versa. Additionally, for hydrate formation, availability of both gas and water in sufficient quantities in the pore-space is a necessary condition. This behavior of A_{rs} is modeled using the parameterization proposed by *Sun and Mohanty* [2006].

The rate of reaction, k_{reac}, is a *free parameter* in our simulation which is used to calibrate the hydrate-kinetics model with respect to the experimental data. In the table we can see that the values of k_{reac}, for both hydrate formation as well as dissociation periods, lie well within the range reported in the literature.

The poroelastic behavior of the hydrate-bearing sediment is characterized by three parameters, viz., *Biot*'s constant α_{biot}, Poisson ratio ν_{sh}, and Young's modulus E_{sh}. Biot's constant is chosen from a range of typically expected values. The Poisson's ratio is assumed to be a constant independent of the hydrate saturation following the experimental studies by *Miyazaki et al*. [2011b]; *Lee et al*. [2010a]. The Young's modulus is modeled using the parameterization proposed by *Santamarina and Ruppel* [2010], given by equation (28). The Young's modulus E_{sh} is a *free parameter* which is used to calibrate the poroelasticity model with respect to the experimental data.

4.4. Simulation Results

As discussed above, we essentially chose *one* free parameter in kinetics, i.e., k_{reac}, and *one* free parameter in linear-elasticity, which is E_{sh}, to calibrate the kinetic and the mechanical models separately. With these calibrated models, we simulate numerically the coupled (thermo-chemo)-hydro-geomechanical response of the sand sample in triaxial test-setting using our gas hydrate reservoir model. The numerical results, together with the corresponding experimental data, are plotted in Figure 9 for the gas hydrate formation period, and in Figure 8 for the hydrate dissociation period.

In the **gas hydrate formation period**, methane gas in the free pore space is continuously consumed and average bulk gas pressure is decreased (see Figure 9a). Clearly, the rate of gas hydrate formation is not constant. In the beginning, after the sample is pressurized at constant isotropic effective stress, gas hydrate formation from free methane gas and pore water is fast, but the rate of formation steadily decreases due to mass transfer limitations and shrinking reaction surfaces. In accordance to that, after pressurization the gas hydrate saturation increases rapidly and the water saturation decreases proportionally (Figure 9b). Note that the reported values of phase saturations are calculated based on initial values and gas pressure measurements. The volumetric strain shows a fast positive response during early gas hydrate formation at relatively low gas hydrate saturations, and sample stiffness increases at higher gas hydrate saturations (Figure 9c). The fast volumetric strain response that occurs at constant apparent effective stress results from changes in

a) Gas pressure P_g at depressurization boundary (at $z = 0$)

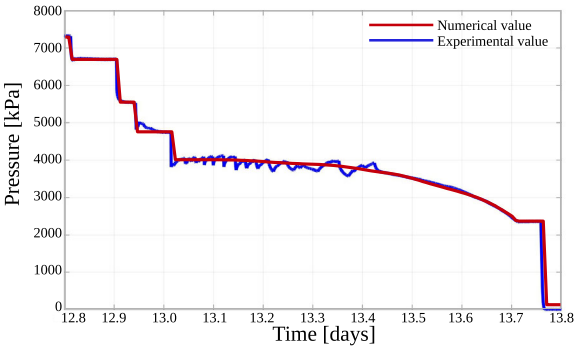

b) Cumulative gas production over time.

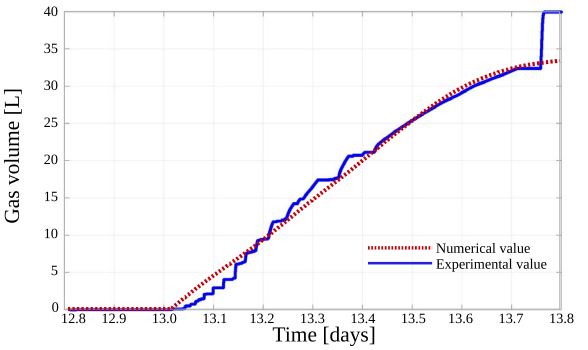

c) Total volumetric strain in the sample over time.
note: '+' value indicates compression.

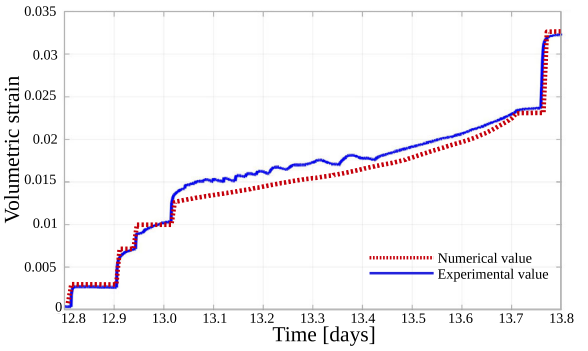

d) Temperature in the sample over time.

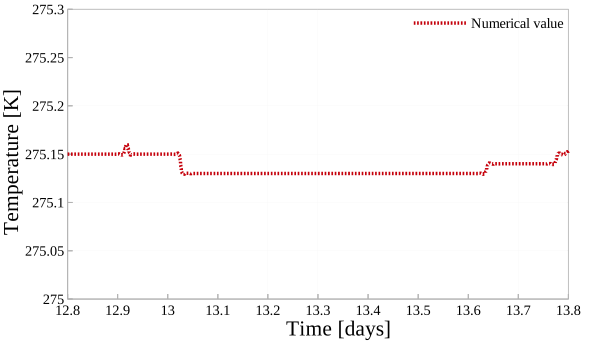

Figure 8. Comparison of the simulation results with the experimental results for the **depressurization and gas production** period. (a) Gas pressure P_g at depressurization boundary (at $z = 0$). (b) Cumulative gas production over time. (c) Total volumetric strain in the sample over time. Note: "+" value indicates compression. (d) Temperature in the sample over time.

a) Average gas pressure P_g in the domain over time.

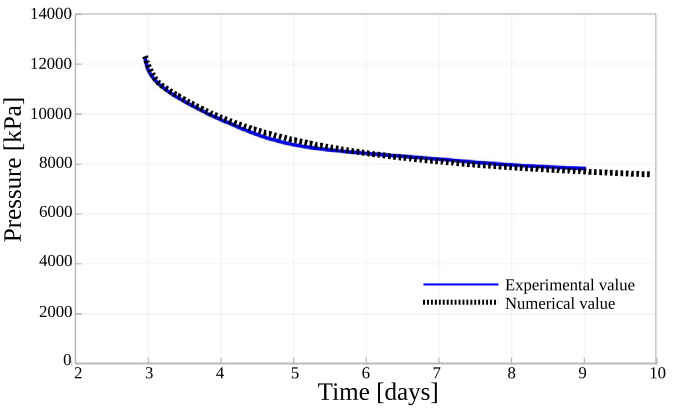

b) Average S_w and S_h in the domain over time.

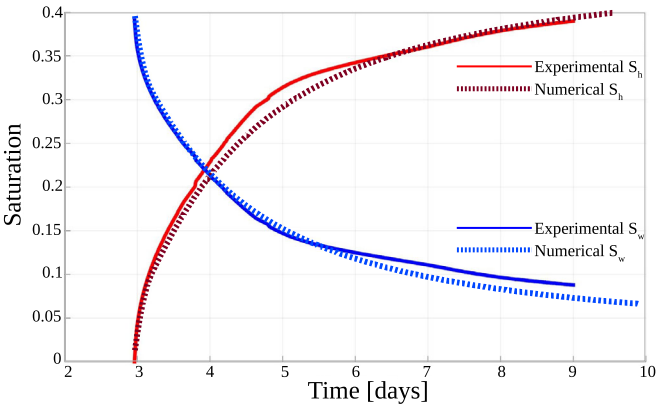

c) Total volumetric strain in the sample over time.
note: '+' value indicates compression.

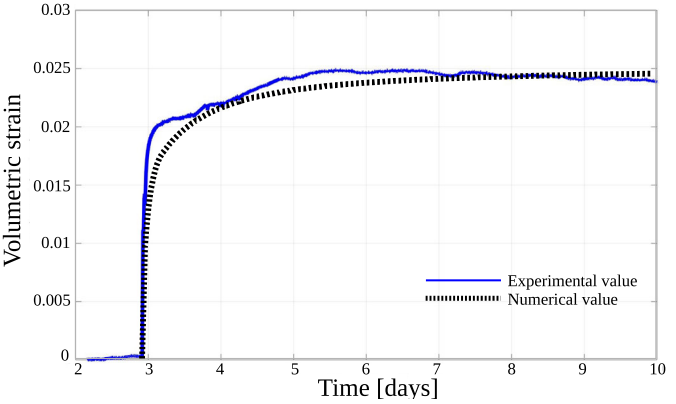

Figure 9. Comparison of the simulation results with the experimental results for the **gas hydrate formation** period. (a) Average gas pressure P_g in the domain over time. (b) Average S_w and S_h in the domain over time. (c) Total volumetric strain in the sample over time. Note: "+" value indicates compression.

water saturation and, thus, capillary pressure, which is not monitored experimentally, but considered in the numerical simulation.

During the **gas hydrate dissociation period**, pressure is decreased step-wise until methane hydrates become unstable at the respective P-/T-conditions. Figure 8a shows the numerically computed gas phase pressure in the

sample. The gas production is plotted in Figure 8b. With the onset of gas hydrate dissociation after reaching the hydrate stability boundary, pressure is maintained at a relatively constant level because hydrate dissociation and gas production equilibrate dependent on experimental and technical conditions.

Volumetric strain during gas hydrate dissociation, plotted in Figure 8c, is dependent on effective stress and gas hydrate saturation through the sample stiffness, which decreases with the ongoing gas hydrate dissociation and gas production.

Figure 8d shows the numerically computed temperature profile of the sample during dissociation. The model predicts that subcooling from gas hydrate dissociation is quite small, which is expected since the experiment was performed under isothermal temperature control.

5. Discussion and Outlook

In our combined experimental-numerical study, we consider dynamic gas hydrate formation and dissociation in sandy sediment under isotropic compressive loading and show that a simplified coupling concept is capable of reproducing the essential bulk physical behavior, including volumetric strain and gas production.

The assumption that the soil is the primary load-bearing constituent is central to our model concept. This assumption is most reasonable for the pore-filling hydrates with low saturations where the hydrates form by nucleating on sediment grain boundaries and grow freely into pore spaces without entering the pore-throats. For hydrates formed in partially water saturated sands, as is the case in our experiment, it is well known that the hydrates nucleate preferentially in the pore-throats and contribute to the sediment stiffness already at low gas hydrate saturations. For hydrate saturations between 0.25 and 0.4, the hydrates are expected to transition toward a load-bearing habit [*Waite et al*., 2009]. In our experiment, we obtain a maximum hydrate saturation of ≈ 0.4. Our numerical results suggest that in *well-consolidated* sands, our assumption of soil forming the primary load-bearing skeleton remains valid even for hydrate saturations which lie in the transition zone between pore-filling and load-bearing habits. We hypothesize that this is because in *well-consolidated* sands, the deformation of hydrates relative to the soil skeleton is quite small in the transition zone. However, for higher hydrate saturations where hydrates become fully load-bearing, we expect strong limitations to this coupling concept. Furthermore, for massive hydrates with saturations exceeding 0.8, we even expect that the hydrate and the soil phases can no longer be modeled as a single composite phase, and new model concepts are necessary to consistently describe the interface conditions between the hydrate and the soil phase boundaries.

Our experiment was focused on analyzing deformation under variable gas hydrate saturation, and a wide range of effective stress loading, controlled between 1 and 9 MPa. To limit the bulk sample deformation and relative grain-to-grain movement only isotropic stresses were applied. Gas hydrates were formed after isotropic consolidation to 1 MPa using the excess-gas-method [*Chong et al*., 2016; *Choi et al*., 2014; *Jin et al*., 2012; *Priest et al*., 2009]. After gas hydrate formation, the remaining gas was fully replaced with seawater. After gas-seawater replacement, the sample was equilibrated for approximately 5 days to allow for gas hydrate alteration before the sample was depressurized. A poroelasticity framework was chosen for describing the mechanical behavior of the sediment in order to minimize the uncertainties arising from unknown mechanical behavior of gas hydrate-bearing sediments. The deliberate choice of a simple constitutive law with a limited number of parameters, in contrast to using more complex elastoplastic modeling approaches, is justified by the design of the experimental test case. It is important to note that, within the constraints of small-strain deformations and pore-filling hydrates, the coupling concept presented here does not depend on the stress-strain constitutive law as such. The concept of poroelasticity is, therefore, sufficient to test the validity of our coupling concept provided that the design of the experiment ensures that the sample deformations remain small and well within elastic limit. For large deformations, the coupling concept is not validated so far.

To approximate our experimental data, we treated the kinetic term k_{reac} in the transport block as a fitting parameter. Similarly, we used fitting of the stiffness model parameters to match the experimental volumetric strain behavior. We chose a functional dependence of composite modulus E_{sh} on hydrate saturation S_h as proposed by *Santamarina and Ruppel* [2010] and other authors [*Rutqvist et al*., 2009; *Klar et al*., 2010, 2013]. Knowledge about mechanical stiffness and strength properties of gas hydrate-bearing sediments is

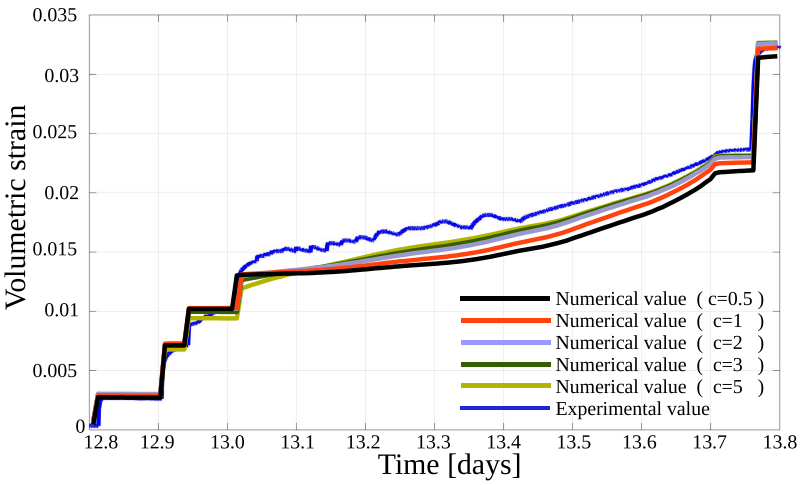

Figure 10. Volumetric strain curves for different functional dependences of E_{sh} on S_h (i.e., $c=1, 2, 3, 5$) for the **depressurization and gas production** period. Note: "+" value indicates compression.

still limited. Experimental analysis of mechanical properties is problematic, because it is equally important to control effective stress conditions and phase saturations, and there are no test procedures available to guarantee homogeneous gas hydrate saturations and full water saturation. Further, mechanical properties are strongly dependent on gas hydrate-sediment fabrics and formation procedures, and effects from dynamic changes in gas hydrate saturation, distributions, and alterations of gas hydrate-sediment fabrics needs further investigation and development of novel test procedures [*Deusner et al*., 2016] particularly for dynamic test scenarios. Overall, the calibrated values for E_{sh} from our study are in accordance with earlier experimental and numerical studies, which reported Young's modulus or secant stiffness in a wide range of approximately 100–400 MPa for relevant gas hydrate concentrations [*Brugada et al*., 2010; *Miyazaki et al*., 2010; *Lee et al*., 2010b; *Yun et al*., 2007]. Although the composite modulus E_{sh} was treated as a free fitting parameter and initialized based on apparent stress-strain behavior during the intervals of known and constant gas hydrate saturations, physically meaningful values for individual modulii E_s and E_h were obtained. E_s for the sediment without gas hydrate reflected stiffness behavior typical for loose soil during gas hydrate formation while the sample was normally consolidated at low effective stress. The results from the numerical simulation suggest that an apparent step-like increase in bulk composite stiffness (i.e., the change of apparent E_{sh} from 132 to 183 MPa) occurred during the time interval between the completion of gas hydrate formation and the start of depressurization. We assume that this response was caused by the high transient effective stress and the composite sediment consolidation, which could not be avoided during the gas-water exchange. In order to accomplish the replacement of gas with water sufficiently fast, and to minimize gas hydrate dissociation during the short time interval of gas-water exchange, the confining stress instead of the apparent effective stress was controlled at a constant value during gas-water exchange. In fitting the model to the experimental data, we adjusted both E_s and E_h rather than constraining the effect of consolidation to one of the parameters a priori. However, the validity of this assumption needs to be further investigated using advanced geotechnical and microstructural analyses. Furthermore, it needs to be considered that the poroelasticity model adopted for testing our coupled numerical simulation scheme does not explicitly consider effective stress-dependent changes in the modulii E_s and E_h, which could also contribute to the apparent differences in E_{sh} during gas hydrate formation and dissociation periods. In our simulation, the composite modulus E_{sh} depends almost linearly on S_h during gas hydrate formation, while during the hydrate dissociation period the dependence of E_{sh} on S_h is smaller. Figure 10 shows the volumetric-strain plotted over time for the depressurization period for different functional dependences of E_{sh} on S_h (i.e., $c=0.5, 1, 2, 3, 5$). Our simulation results indicate that an exponent $c=3$ is a reasonable approximation. *Santamarina and Ruppel* [2010] suggest that S_h tends to be raised to a power larger than 1, which reduces the impact on stiffness at low gas hydrate saturations relative to that for high gas hydrate saturations. Since gas hydrates formed using the excess-gas-method are predominantly located in the pore throats rather than in the free pore space, the linear and relatively stronger dependence of E_{sh} on S_h during formation appears reasonable. The weaker dependence of E_{sh} on gas hydrate saturation during dissociation is also

reasonable, since after exchanging gas with water in the pore space, gas hydrate-sediment fabrics were allowed to alter, and also during dissociation the grain-scale hydrate-sand structure is necessarily changed. Thus, our results clearly show that dynamic structural transitions in gas hydrate-bearing sediments during gas hydrate formation, aging, and dissociation can have substantial effects on sediment mechanical properties. Further combined experimental-numerical studies with the objective to simulate the geomechanical effects from such dynamic changes in gas hydrate-sediment fabrics are currently ongoing.

Acknowledgments
We gratefully acknowledge the support for the first author by the German Research Foundation (DFG), through project WO 671/11-1. This work was further funded by the German Federal Ministries of Economy (BMWi) and Education and Research (BMBF) through the SUGAR project (grant 03SX250, 03SX320A, and 03G0856A), and the EU-FP7 project MIDAS (grant agreement 603418). The reported experimental data are attached as supporting information with this article.

References

Ahmadi, G., C. Ji, and H. Duane (2004), Numerical solution for natural gas production from methane hydrate dissociation, *J. Pet. Sci. Eng.*, *41*, 169–185.

Anderson, B., R. Boswell, C. T.S., H. Farrell, S. Ohtsuki, M. White, and M. Zyrianova (2014), Review of the findings of the ignik sikumi co2-ch4 gas hydrate exchange field trial, in *Proceedings of the 8th International Conference on Gas Hydrates*, ICGH8, Beijing, China.

Archer, D., B. Buffett, and V. Brovkin (2009), Ocean methane hydrates as a slow tipping point in the global carbon cycle, *Proc. Natl. Acad. Sci. U. S. A.*, *106*, 20,596–20,601.

Biot, M. (1941), General theory of three-dimensional consolidation, *J. Appl. Phys.*, *12*, 155–164.

Biot, M., and D. Willis (1957), The elastic coefficients of the theory of consolidation, *J. Appl. Mech.*, *24*, 594–601.

Brugada, J., Y. Cheng, K. Soga, and J. Santamarina (2010), Discrete element modelling of geomechanical behaviour of methane hydrate soils with pore-filling hydrate distribution, *Granul. Matter*, *12*(5), 517–525, doi:10.1007/s10035-010-0210-y.

Burdine, N. T. (1953), Relative permeability calculations from pore-size distribution data, *J. Petrol. Tech.*, *5*(3), 71–78.

Burwicz, E., L. Rüpke, and K. Wallmann (2011), Estimation of the global amount of submarine gas hydrates formed via microbial methane formation based on numerical reaction-transport modeling and a novel parameterization of holocene sedimentation, *Geochim. Cosmochim. Acta*, *75*, 4562–4576.

Choi, J., S. Dai, J. Cha, and Y. Seol (2014), Laboratory formation of noncementing hydrates in sandy sediments, *Geochem. Geophys. Geosyst.*, *15*, 1648–1656, doi:10.1002/2014GC005287.

Chong, Z., M. Yang, B. Khoo, and P. Linga (2016), Size effect of porous media on methane hydrate formation and dissociation in an excess gas environment, *Ind. Eng. Chem. Res.*, *55*(29), 7981–7991.

Civan, F. (2000), Predictability of porosity and permeability alterations by geochemical and geomechanical rock and fluid interactions, in *SPE 58746 International Symposium on Formation Damage Control*, pp. 359–370, Society of Petroleum Engineers, Richardson, Tex., doi: 10.2118/58746-MS. [Available at www.onepetro.org/doi/10.2118/58746-MS.]

David, C. (2013), Japanese test coaxes fire from ice, *Nature*, *496*, 409, doi:10.1038/496409a.

Dedner, A., B. Flemisch, and R. Klöfkorn (2012), *Advances in DUNE: Proceedings of the DUNE User Meeting, Held in October 6th–8th 2010 in Stuttgart, Germany*, Springer, Berlin.

Demmel, J., J. Gilbert, and X. Li (1999), Superlu users' guide, *Tech. Rep. LBNL-44289*, Lawrence Berkeley Natl. Lab., Berkeley, Calif.

Deusner, C., N. Bigalke, E. Kossel, and M. Haeckel (2012), Methane production from gas hydrate deposits through injection of supercritical CO_2, *Energies*, *5*(7), 2112–2140, doi:10.3390/en5072112.

Deusner, C., S. Gupta, E. Kossel, M. Freise, H. Anbergen, T. Wille, N. Bigalke, and M. Haeckel (2016), The role of high-pressure flow-through experiments for evaluating the mechanical behaviour of gas hydrate-bearing soils, in *Energy Geotechnics*, edited by F. Wuttke, S. Bauer, and M. Sanchez, pp. 437–443, CRC Press, Taylor and Francis Group, London, U. K., doi:10.1201/b21938-70.

Esmaeilzadeh, F., M. E. Zeighami, and J. Fathi (2008), 1-D modeling of hydrate decomposition in porous media, *Int. J. Chem. Molec. Nucl. Mater. Metall. Eng.*, *2*(5), 45–51.

Friend, D. G., J. F. Ely, and H. Ingham (1989), Thermophysical properties of methane, *J. Phys. Chem. Ref. Data*, *18*(2), 583–638, doi:https://doi.org/10.1063/1.555828.

Gupta, S., R. Helmig, and B. Wohlmuth (2015), Non-isothermal, multi-phase, multi-component flows through deformable methane hydrate reservoirs, *Comput. Geosci.*, *19*, 1–26, doi:10.1007/s10596-015-9520-9.

Gupta, S., B. Wohlmuth, and R. Helmig (2016), Multi-rate time stepping schemes for hydro-geomechanical model for subsurface methane hydrate reservoirs, *Adv. Water Resour.*, *91*, 78–87.

Hager, C., and B. Wohlmuth (2009), Nonlinear complementarity functions for plasticity problems with frictional contact, *Comput. Methods Appl. Mech. Eng.*, *198*(41), 3411–3427, doi:10.1016/j.cma.2009.06.021.

Hager, C., and B. Wohlmuth (2010), Semismooth newton methods for variational problems with inequality constraints, *GAMM Mitt.*, *33*, 8–24.

Helmig, R. (2016), *Multiphase Flow and Transport Processes in the Subsurface: A Contribution to the Modeling of Hydrosystems*, vol. 91, pp. 78–87, Springer, Berlin.

Himmelblau, D. M. (1964), Diffusion of dissolved gases in liquids, *Chem. Rev.*, *64*(5), 527–550.

Hyodo, M., Y. Li, J. Yoneda, Y. Nakata, N. Yoshimoto, and A. Nishimura (2014), Effects of dissociation on the shear strength and deformation behavior of methane hydrate-bearing sediments, *Mar. Petrol. Geol.*, *51*, 52–62, doi:10.1016/j.marpetgeo.2013.11.015.

Janicki, G., S. Schlüter, T. Hennig, H. Lyko, and G. Deerberg (2011), Simulation of methane recovery from gas hydrates combined with storing carbon dioxide as hydrates, *J. Geol. Res.*, *2011*, 462156, 1–15, doi:10.1155/2011/462156.

Jin, Y., Y. Konno, and J. Nagao (2012), Growth of methane clathrate hydrates in porous media, *Energy Fuels*, *26*(4), 2242–2247.

Kamath, V. A. (1984), Study of heat transfer characteristics during dissociation of gas hydrates in porous media, PhD thesis, Univ. of Pittsburgh, Pittsburgh, Pa.

Kamath, V. A., and G. D. Holder (1987), Dissociation heat transfer characteristics of methane hydrates, *AIChE J.*, *33*, 347–350.

Kim, H., P. Bishnoi, R. Heidemann, and S. Rizvi (1987), Kinetics of methane hydrate decomposition, *Chem. Eng. Sci.*, *42*(7), 1645–1653, doi: 10.1016/0009-2509(87)80169-0.

Kimoto, S., F. Oka, and T. Fushita (2010), A chemo-thermo-mechanically coupled analysis of ground deformation induced by gas hydrate dissociation, *Int. J. Mech. Sci.*, *52*(2), 365–376.

Klar, A., K. Soga, and M. Y. Ng (2010), Coupled deformation-flow analysis for methane hydrate extraction, *Geotechnique*, *60*(10), 765–776, doi:10.1680/geot.9.P.079-3799.

Klar, A., S. Uchida, K. Soga, and K. Yamamoto (2013), Explicitly coupled thermal flow mechanical formulation for gas-hydrate sediments, *SPE J.*, *18*, 196–206.

Kurihara, M., A. Sato, H. Ouchi, H. Narita, Y. Masuda, T. Saeki, and T. Fujii (2009), Prediction of gas productivity from eastern nankai trough methane-hydrate reservoirs, *SPE125481*, *SPE Reserv. Eval. Eng.*, *12*, 477–499.
Kvenvolden, K. (1993), Gas hydrates, geological perspective and global change, *Rev. Geophys.*, *31*, 173–187.
Lee, H., Y. Seo, Y.-T. Seo, I. Moudrakovski, and J. Ripmeester (2003), Recovering methane from solid methane hydrate with carbon dioxide, *Angew. Chem. Int. Ed.*, *42*, 5048–5051.
Lee, J. Y., F. Francisca, J. Santamarina, and C. Ruppel (2010a), Parametric study of the physical properties of hydrate-bearing sand, silt, and clay sediments: 2. small-strain mechanical properties, *J. Geophys. Res.*, *115*, B11105, doi:10.1029/2009JB006670.
Lee, J. Y., J. C. Santamarina, and C. Ruppel (2010b), Volume change associated with formation and dissociation of hydrate in sediment, *Geochem. Geophys. Geosyst.*, *11*, Q03007, doi:10.1029/2009GC002667.
Lin, J.-S., Y. Seol, and J. H. Choi (2015), An SMP critical state model for methane hydrate-bearing sands, *Int. J. Numer. Anal. Methods Geomech.*, *39*(9), 969–987, doi:10.1002/nag.2347.
Liu, X., and P. Flemings (2007), Dynamic multiphase flow model of hydrate formation in marine sediments, *J. Geophys. Res.*, *112*, B03101, doi:10.1029/2005JB004227.
Mielke, A. (2004), Existence of minimizers in incremental elasto-plasticity with finite strains, *SIAM J. Math. Anal.*, *36*(2), 384–404.
Mielke, A. (2009), Global existence for rate-independent gradient plasticity at finite strain, *J. Nonl. Sci.*, *19*(3), 221–248.
Milkov, A. V. (2004), Global estimates of hydrate-bound gas in marine sediments: How much is really out there?, *Earth Sci. Rev.*, *66*(3–4), 183–197, doi:10.1016/j.earscirev.2003.11.002.
Miyazaki, K., A. Masui, K. Aoki, Y. Sakamoto, T. Yamaguchi, and S. Okubo (2010), Strain-rate dependence of triaxial compressive strength of artificial methane-hydrate-bearing sediment, *Int. J. Offshore Polar Eng.*, *20*(4), 256–264.
Miyazaki, K., et al. (2011a), Application of nonlinear elastic constitutive model to analysis of artificial methane-hydrate-bearing sediment sample, in *Ninth ISOPE Ocean Mining Symposium*, Int. Soc. Offshore and Polar Eng., pp. 15–20, Maui, Hawaii.
Miyazaki, K., A. Masui, Y. Sakamoto, K. Aoki, N. Tenma, and T. Yamaguchi (2011b), Triaxial compressive properties of artificial methane-hydrate-bearing sediment, *J. Geophys. Res.*, *116*, B06102, doi:10.1029/2010JB008049.
Miyazaki, K., N. Tenma, K. Aoki, and T. Yamaguchi (2012), A nonlinear elastic model for triaxial compressive properties of artificial methane-hydrate-bearing sediment samples, *Energies*, *5*(10), 4057–4075.
Moridis, G. J. (2003), Numerical studies of gas production from methane hydrates, *SPE 87330, SPE J.*, *32*(8), 359–370.
Moridis, G. J., M. Kowalsky, and K. Pruess (2007), Depressurization-induced gas production from class-i hydrate deposits, *SPE J.*, *10*(5), 458–481.
Moridis, G. J., M. Kowalsky, and K. Pruess (2008), *TOUGH-Fx/HYDRATE v1.0 User's manual: A Code for the Simulation of System Behaviour in Hydrate-Bearing Geologic Media*, Earth Sci. Div., Lawrence Berkeley Natl. Lab., Berkeley, Calif.
Moridis, G. J., T. Collett, R. Boswell, M. Kurihara, M. Reagan, C. Koh, and E. Sloan (2009), Toward production from gas hydrates: Current status, assessment of resources, and simulation-based evaluation of technology and potential, *SPE J.*, *12*, 745–771.
Moridis, G. J., et al. (2011), Challenges, uncertainities and issues facing gas production from gas hydrate deposits, *SPE J.*, *14*, 76–112.
Park, Y., D.-Y. Kim, J.-W. Lee, D.-G. Huh, K.-P. Park, J. Lee, and H. Lee (2006), Sequestering carbon dioxide into complex structures of naturally occurring gas hydrates, *Proc. Natl. Acad. Sci. U. S. A.*, *103*, 12,690–12,694.
Peng, D. Y., and D. B. Robinson (1976), A new two-constant equation of state, *Ind. Eng. Chem.*, *15*, 59–64, doi:10.1021/i160057a011.
Piñero, E., M. Marquardt, C. Hensen, M. Haeckel, and K. Wallmann (2013), Estimation of the global inventory of methane hydrates in marine sediments using transfer functions, *Biogeosciences*, *10*(2), 959–975.
Priest, J. A., E. V. L. Rees, and C. R. I. Clayton (2009), Influence of gas hydrate morphology on the seismic velocities of sands, *J. Geophys. Res.*, *114*, B11205, doi:10.1029/2009JB006284.
Rockhold, M., R. Yarwood, M. Niemet, P. Bottomley, and J. Selker (2002), Considerations for modelling bacterial-induced changes in hydraulic properties of variably sarurated porous media, *Adv. Water Resour.*, *25*, 477–495.
Roder, H. (1985), Thermal conductivity of methane for temperatures between 110 k and 310 k with pressures up to 70 mpa, *J. Thermophys.*, *6*(2), 119–142.
Rutqvist, J. (2011), Status of the tough-flac simulator and recent applications related to coupled fluid flow and crustal deformations, *Comput. Geosci.*, *37*, 739–750, doi:10.1016/j.cageo.2010.08.006.
Rutqvist, J., G. Moridis, T. Grover, and T. Collett (2009), Geomechanical response of permafrost-associated hydrate deposits to depressurization-induced gas production, *J. Petrol. Sci. Eng.*, *67*(1–2), 1–12, doi:10.1016/j.petrol.2009.02.013.
Sander, R. (2015), Henry's law constants, in *NIST Chemistry WebBook*, edited by P. Linstrom and W. Mallard, no. 69 in NIST Standard Reference Database, Natl. Inst. of Stand. and Technol., Gaithersburg, Md., retrieved 23 Feb.
Santamarina, J. C., and C. Ruppel (2010), The impact of hydrate saturation on the mechanical, electrical, and thermal properties of hydrate-bearing sand, silts, and clay, in *Geophysical Characterization of Gas Hydrates, Geo-phys. Dev. Ser.*, *vol.* 14, edited by M. Riedel, C. Willoughby, and S. Chopra, pp. 373–384, Soc. of Explor. Geophys., Tulsa, Okla.
Schoderbek, D., H. Farrell, K. Hester, J. Howard, K. Raterman, S. Silpngarmlert, K. Martin, B. Smith, and P. Klein (2013), Conocophillips gas hydrate production test final technical report, technical report SciTech Connect, ConocoPhillips.
Sloan, E., and C. Koh (2007), *Clathrate Hydrates of Natural* Gases, 3rd ed., *Chemical* Industries, CRC Press, Taylor and Francis Group, Boca Raton, Fla.
Stattery, J., and R. Bird (1958), Calculation of diffusion coefficient of dilute gases and of the self-diffusion coefficient of dense gases, *AIChE J.*, *4*(2), 137–142.
Stern, L. A., S. Circone, S. H. Kirby, and W. B. Durham (2003), Temperature, pressure, and compositional effects on anomalous or ''self'' preservation of gas hydrates, *Can. J. Phys.*, *81*(1–2), 271–283, doi:10.1139/p03-018.
Sun, F., and K. Mohanty (2006), Kinetic simulation of methane hydrate formation and dissociation in porous media, *Chem. Eng. Sci.*, *61*, 3476–3495.
Sun, F., K. Mohanty, and N. Nanchary (2005), 1-d modelling of hydrate depressurization in porous media, *Transp. Porous Media*, *58*, 315–338.
Sun, X., X. Guo, L. Shao, and H. Tang (2015), A thermodynamics-based critical state constitutive model for methane hydrate bearing sediment, *J. Nat. Gas Sci. Eng.*, *27*(2), 1024–1034, doi:10.1016/j.jngse.2015.09.048.
Terzaghi, K. (1925), *Erdbaumechanik auf Bodenphysikalischer Grundlage*, F. Deuticke, Wien.
Tsypkin, G. (1991), Effect of liquid phase mobility on gas hydrate dissociation in reservoirs, *Izv. Akad. Nauk. SSSR. Mekh. Zhidkosti i Gaza.*, *4*, 105–114.
Uchida, S., K. Soga, and K. Yamamoto (2012), Critical state soil constitutive model for methane hydrate soil, *J. Geophys. Res.*, *117*, B03209, doi:10.1029/2011JB008661.

Verruijt, A. (2008), *Encyclopedia of Hydrological Sciences*, chap. Consolidation of Soils, John Wiley, Chichester, U. K., doi:10.1002/0470848944.hsa303.

Wagner, W., and H.-J. Kretzschmar (2008), Iapws industrial formulation 1997 for the thermodynamic properties of water and steam, in *International Steam Tables: Properties of Water and Steam Based on the Industrial Formulation IAPWS-IF97*, pp. 7–150, Springer, Berlin Heidelberg, doi:10.1007/978-3-540-74234-0_3.

Waite, W. F., et al. (2009), Physical properties of hydrate-bearing sediments, *Rev. Geophys.*, *47*, RG4003, doi:10.1029/2008RG000279.

White, M. D., and B. P. McGrail (2006), Stomp-hyd: A new numerical simulator for analysis of methane hydrate production from geologic formations, in *Proceedings of 2nd International Symposium on Gas Hydrate Technology at the 43rd Coordinating Committee for Geoscience Programmes in East and Southeast Asia (CCOP) Annual Session, October 29–November 3*, edited by J. B. A Reedman, Y. S. Park, and N. Chaimanee, pp. 77–86, The Coordinating Committee for Geoscience Programmes in East and Southeast Asia (CCOP), Bangkok, Thailand.

Yamamoto, K. (2013), Japan completes first offshore methane hydrate production test - methane successfully produced from deepwater hydrate layers, Fire in the ice: Department of energy, office of fossil energy, national energy technology laboratory, *Methane Hydrate Newslett.*, *13*(1–2).

Yamamoto, K. (2015), Overview and introduction: Pressure core-sampling and analyses in the 2012–2013 mh21 offshore test of gas production from methane hydrates in the eastern nankai trough, *Mar. Pet. Geol.*, *66*, 296–309.

Yousif, M. (1991), Experimental and theoretical investigation of methane-gas-hydrate dissociation in porous media, *SPE J.*, *6*(1), 69–76.

Yu, F., Y. Song, W. Liu, Y. Li, and W. Lam (2011), Analyses of stress strain behavior and constitutive model of artificial methane hydrate, *J. Petrol. Sci. Eng.*, *77*(2), 183–188, doi:10.1016/j.petrol.2011.03.004.

Yun, T., J. Santamarina, and C. Ruppel (2007), Mechanical properties of sand, silt, and clay containing tetrahydrofuran hydrate, *J. Geophys. Res.*, *112*, B04106, doi:10.1029/2006JB004484.